Proceedings of the 28th IEEE
EMBS Annual International Conference
New York City, USA, Aug 30-Sept 3, 2006

MicroCT-guided Bioluminescence Tomography Based on the Adaptive Finite Element Tomographic Algorithm

Yujie Lv, Jie Tian*, *Senior member, IEEE*, Wenxiang Cong, Ge Wang, *Fellow, IEEE*, and Durairaj Kumar

***Abstract*— Molecular imaging is an emerging imaging technique in biological and medical field. Thereinto, bioluminescence tomography (BLT) plays a significant role. In view of the ill-posedness of the BLT problem, *a priori* knowledge is indispensable to reconstruct bioluminescent source uniquely and quantitatively. In this paper, the anatomical information of a real mouse is obtained with the microCT scanner to represent different macroscopic biological tissues. The proposed tomographic algorithm based on the adaptive finite element methods (FEMs) employs the microCT slices based coarse volumetric mesh to reconstruct source distribution quantitatively according to *a posteriori* error estimation techniques. In order to avoid the *inverse crime*, a Monte Carlo (MC) method based virtual optical environment, molecular optical simulation environment (MOSE), is also adopted for producing the measurement data. Finally, simulation results with the above framework demonstrate the effectiveness and potential of the proposed adaptive tomographic algorithm.**

I. INTRODUCTION

Molecular imaging, especially small-animal molecular imaging, is an active research field[1]. Photonics-based imaging modalities have become the important tools to reveal the molecular and cellular information *in vivo*, including bioluminescence tomography (BLT)[2], fluorescence molecular tomography (FMT)[3], and so on. Their mechanism is to identify light source from light flux detected on the surface of a small animal, which has been used for tumorigenesis and metastasis, drug discovery, and gene therapy *etc.*[4]. Compared with the traditional structural and functional imaging methods such as computed tomography (CT), magnetic resonance imaging (MRI) and positron emission tomography (PET), BLT and FMT can obtain functional and spatial information simultaneously with much higher imaging contrast and sensitivity, which is beneficial from the optical reporters linked to the tissue-specific target[4].

In theory, bioluminescence tomography is more ill-posed than fluorescence molecular tomography due to the absence of the external exciting source[1]. The uniqueness research on BLT shows that *a priori* knowledge has a quite important effect in source reconstruction, such as the anatomical information and the optical properties of small animal, the spectrum characteristic of bioluminescent source, and so on[5], [6]. Although the finite element based tomographic algorithms have been developed[7], there is always the contradiction between the reconstruction time costing and the discretization degree of the given domain. In principle, the finer the discretized mesh is, the more precise the BLT solution is, and yet the longer the time costing is.

Ground on the consideration of the above problems, a real mouse is scanned by the microCT scanner with capacity of $20-100\mu m$ spatial resolution and then the volumetric finite element mesh is reconstructed with the mouse slices via a series of operations. A novel tomographic algorithm is proposed based on the adaptive finite element methods (FEMs) to reconstruct source distribution quantitatively using *a posteriori* error estimation. This diffusion equation based method also utilizes *a priori* knowledge to decide the permissible source region[7]. In the adaptive procedure, the optimization is done using a modified Newton method coupled with the active-set strategy. With the purpose of exploring the performance of the proposed algorithm and avoiding the *inverse crime*, molecular optical simulation environment (MOSE)[8], which is researched and developed to model bioluminescent photon transportation in the living mouse, is adopted to produce the synthetic data. The final computational results show the effectiveness of the adaptive finite element based tomographic algorithm.

II. METHODS

A. Diffusion approximation and boundary condition

In bioluminescence tomography, the diffusive photon propagation is depicted by the steady-state diffusion equation and Robin boundary condition[7]:

$$-\nabla\cdot\big(D(\mathbf{x})\nabla\Phi(\mathbf{x})\big)+\mu_a(\mathbf{x})\Phi(\mathbf{x})=S(\mathbf{x})\ (\mathbf{x}\in\Omega) \quad (1\text{-}1)$$

$$\Phi(\mathbf{x})+2A(\mathbf{x};n,n')D(\mathbf{x})\big(\mathbf{v}(\mathbf{x})\cdot\nabla\Phi(\mathbf{x})\big)=0\ (\mathbf{x}\in\partial\Omega) \quad (1\text{-}2)$$

where $\Phi(\mathbf{x})$ denotes the photon flux density$[Watts/mm^2]$; $S(\mathbf{x})$ is the source energy density $[Watts/mm^3]$; $\mu_a(\mathbf{x})$ is the absorption coefficient$[mm^{-1}]$; $D(\mathbf{x})$=$1/(3(\mu_a(\mathbf{x})+(1-g)\mu_s(\mathbf{x})))$ is the optical diffusion coefficient$[mm^{-1}]$, $\mu_s(\mathbf{x})$ the scattering coefficient$[mm^{-1}]$, g the anisotropy parameter.

When the bioluminescence imaging experiment is performed in a dark environment, (1-2) represents the boundary condition between the medium and the mouse, where **v** is the unit outer normal on $\partial\Omega$. Considering the mismatch between the refractive indices n for Ω and n' for the external medium,

This work is supported by NSFDYS(60225008), NSFC(30370418, 90209008, 60302016, 60532050 and 30500131), JRFOCYS(30528027) and BNSF(4051002 and 4042024) in China and in part by an NIH/NIBIB grant EB001685.

Y. Lv and J. Tian are with Medical Image Processing Group, Institute of Automation, Chinese Academy of Sciences, P. O. Box 2728, Beijing 100080, China, e-mail: tian@ieee.org

W. Cong, G. Wang and D. Kumar are with Bioluminescence Tomography Laboratory, Department of Radiology, University of Iowa, Iowa City, Iowa 52242, USA, e-mail: ge-wang@ieee.org

$A(\mathbf{x};n,n')$ can be approximately represented:

$$A(\mathbf{x};n,n') \approx \frac{1+R(\mathbf{x})}{1-R(\mathbf{x})} \tag{2}$$

where n' is close to 1.0 when the experimental environment is in air, $R(\mathbf{x})$ can be approximated by $R(\mathbf{x}) \approx -1.4399n^{-2}+0.7099n^{-1}+0.6681+0.0636n$[7]. The measured quantity is the outgoing flux density on $\partial\Omega$:

$$Q(\mathbf{x}) = -D(\mathbf{x})\big(\mathbf{v}\cdot\nabla\Phi(\mathbf{x})\big) = \frac{\Phi(\mathbf{x})}{2A(\mathbf{x};n,n')} \ (\mathbf{x}\in\partial\Omega) \tag{3}$$

B. Reconstruction method based on the adaptive FEMs

Based on the finite element theory[9], The weak solution of the flux density $\Phi(\mathbf{x})$ is given with (1-1) and (1-2):

$$\int_\Omega \Big(D(\mathbf{x})\big(\nabla\Phi(\mathbf{x})\big)\cdot\big(\nabla\Psi(\mathbf{x})\big)+\mu_a(\mathbf{x})\Phi(\mathbf{x})\Psi(\mathbf{x})\Big)\mathrm{d}\mathbf{x} + \int_{\partial\Omega}\frac{1}{2A_n(\mathbf{x})}\Phi(\mathbf{x})\Psi(\mathbf{x})\mathrm{d}\mathbf{x} = \int_\Omega S(\mathbf{x})\Psi(\mathbf{x})\mathrm{d}\mathbf{x} \tag{4}$$

Furthermore, under the theory framework of the adaptive finite element methods, let $\{\mathcal{T}_1,...\mathcal{T}_k,...\}$ be a sequence of nested triangulation of the given domain Ω based on the adaptive mesh refinement, where the sequence gradually changes from coarse to fine along with an increase in k. The spaces of linear finite elements $\mathcal{V}_k$ are introduced on the discretized levels $\mathcal{T}_k$, satisfying $\mathcal{V}_1 \subset ... \subset \mathcal{V}_k \subset ... \subset H^1(\Omega)$. Now, we only consider the kth discretized level which includes $N_{\mathcal{T}_k}$ elements and $N_{\mathcal{P}_k}$ vertex nodes. $\{\psi_1^k,...,\psi_{N_{P_k}}^k\}$ is the nodal basis of the space $\mathcal{V}_k$. $\Phi_k(\mathbf{x})$ is an approximation of $\Phi(\mathbf{x})$ on the kth discretized level:

$$\Phi_k(\mathbf{x}) = \sum_{i=1}^{N_{P_k}} \phi_i^k\psi_i^k(\mathbf{x}) \tag{5}$$

where ϕ_i^k is the ith nodal value. Let $\{\gamma_1^k,...,\gamma_{N_{S_k}}^k\}$ be the interpolation basis function, $S(\mathbf{x})$ is approximated by $S_k(\mathbf{x})$:

$$S_k(\mathbf{x}) = \sum_{i=1}^{N_{S_k}} s_i^k\gamma_i^k(\mathbf{x}) \tag{6}$$

where N_{S_k} and s_i^k are the number of the interpolation basis functions and the interpolation nodal values. We incorporate (5) and (6) with (4) and assemble over all the elements after the integral, the matrix form of (4) is as follows:

$$(K_k+C_k+B_k)\Phi_k = M_k\Phi_k = F_kS_k \tag{7}$$

where the components of the above matrices are given by

$$\begin{cases} k_{ij}^{(k)} = \int_\Omega D(\mathbf{x})\big(\nabla\psi_i^k(\mathbf{x})\big)\cdot\big(\nabla\psi_j^k(\mathbf{x})\big)\mathrm{d}\mathbf{x} \\ c_{ij}^{(k)} = \int_\Omega \mu_a(\mathbf{x})\psi_i^k(\mathbf{x})\psi_j^k(\mathbf{x})\mathrm{d}\mathbf{x} \\ b_{ij}^{(k)} = \int_{\partial\Omega}\psi_i^k(\mathbf{x})\psi_j^k(\mathbf{x})/\big(2A(\mathbf{x};n,n')\big)\mathrm{d}\mathbf{x} \\ f_{ij}^{(k)} = \int_\Omega \psi_i^k(\mathbf{x})\gamma_j^k(\mathbf{x})\mathrm{d}\mathbf{x} \end{cases} \tag{8}$$

Let Φ_k^m and S_k^p denote the boundary measured nodal flux density and the permissible source region respectively. Then, we define the kth level objective function $\Theta_k(S_k^p)$ with Tikhonov regularization method:

$$\Theta_k(S_k^p) = \min_{S_{inf}^k \le S_k^p \le S_{sup}^k} \Big\{\|A_kS_k^p - b_k\|_\Lambda + \lambda_k\eta_k\big(S_k^p\big)\Big\} \tag{9}$$

where S_{inf}^k and S_{sup}^k are the kth level lower and upper bounds; $A_k = F_{11}^{(k)} - M_{12}^{(k)}M_{22}^{-1(k)}F_{21}^{(k)}$ and $b_k = \big(M_{11}^{(k)} - M_{12}^{(k)}M_{22}^{-1(k)}M_{12}^{T(k)}\big)\cdot\Phi_k^m$ have been explained on [7]; $\|\cdot\|_\Lambda$ is the weight matrix, $\|V\|_\Lambda = V^T\Lambda V$; λ_k the regularization parameter and $\eta_k(\cdot)$ the penalty function.

C. Relevant issues

The flowchart of the adaptive tomographic algorithm is shown in Fig. 1. The relevant issues are further demonstrated as follows:

Optimization method: $\Theta_k(S_k^p)$ is a least-square problem with simple bounds, which may be optimized by the box-constrained quadratic programming algorithm. The modified Newton method with the active-set strategy has been adopted to deal with the problem effectively[10] and also employed in each level.

Level switch and convergence criterion: We select the norm of the gradient $\| g_{\Theta_k}^i \|$ and the distance between the last two steps $\| d_{S_k}^i \|$ as the level switch indexes, where $g_{\Theta_k}^i = \nabla\Theta_k(S_k^i)$ and $d_{S_k}^i = S_k^i - S_k^{i-1}$. $\varepsilon_g^{(k)}$ and $\varepsilon_d^{(k)}$ denote the corresponding thresholds. When $\| g_{\Theta_k}^i \|$ is less than $\varepsilon_g^{(k)}$ or $\| d_{S_k}^i \|$ is less than $\varepsilon_d^{(k)}$, the mesh refinement will be triggered. In addition, we utilize the error between the measured and computational boundary nodal flux density or the maximum number of the mesh refinement to terminate the whole reconstruction procedure, that is, $\| \Phi_k^m - \Phi_k^c \| < \varepsilon_\Phi$ or $k \ge L_{max}$.

Error estimation: Two different *a posteriori* error estimates are employed in the forbidden and permissible source region of the object. In the permissible source region, we select r_p of the elements with higher reconstructed values

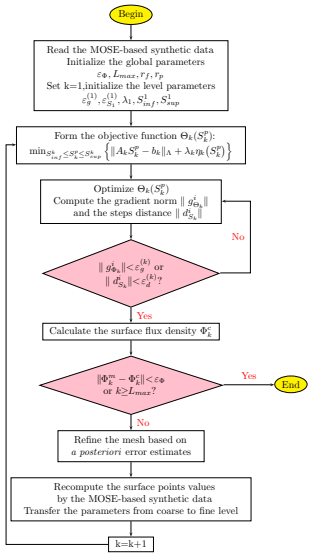

Fig. 1. The flowchart of the adaptive finite element tomographic algorithm.

on the coarse mesh level to refine. Based on the hierarchical defect correction technique[11], the r_f elements are chosen for refinement in the forbidden region.

Mesh refinement: We choose tetrahedron as the basis element of the mesh which is popular in biomedical research field. After selecting the triangulation mode, the local mesh refinement is firstly implemented through the so-called *red refinement*, which divides a tetrahedron into the eight son tetrahedral elements[12]. Following *red refinement*, the irregular refinement *green closure* is used to close the triangulation for consistence. *Red refinement* coupled with *green closure* accomplishes the local mesh refinement reasonably.

D. Utilization of microCT images

In view of the optical properties of biological tissues, the living small animal is a highly heterogeneous object. Although the microCT can't obtain the optical property map, the scanned anatomical information as *a priori* knowledge is significant to BLT source reconstruction[5], [13]. The use of the background optical properties corresponding to the anatomical structure greatly reduces the ill-posedness of the BLT problem and improves the numerical stability and efficiency[5]. In addition, the location and size of the permissible source region can be preferably inferred when the microCT based anatomical information is in cooperation with the surface light power distribution of the small animal and the peak intensity and full width at half maximum (FWHM) change depending on the source depth in different tissues[14].

In BLT reconstruction algorithm, the precise anatomical segmentation is not probably necessary. The aim of BLT is to reconstruct bioluminescent source distribution. In this work, the thorax microCT images of a real mouse is manually segmented into different tissue organs, including lung, bone, heart, liver and muscle. The coarse volumetric mesh built from the segmented images is preferable to the from-coarse-to-fine mesh evolution of the adaptive tomographic algorithm, which can be obtained in turn through surface reconstruction, smooth, simplification, and volumetric finite-element generation after segmentation[15]. The results of key steps are shown in Fig. 2.

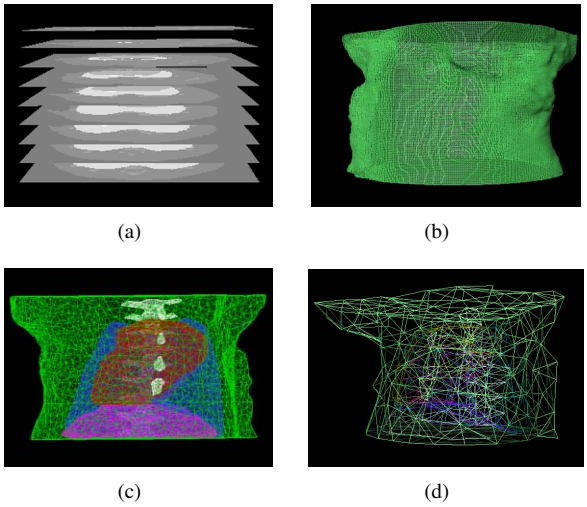

Fig. 2. The key steps of the mesh generation with microCT images. (a) The manually segmented slices; (b) The organs surface reconstruction; (c) The simplified surface mesh used in MOSE; (d) The coarse volumetric mesh used in the adaptive tomographic algorithm.

III. Results

A. Synthetic data production

Monte Carlo method is very popular with the accuracy and flexibility in the photon transportation simulation. The prominent feature of MC method is that Poisson noise is incorporated into the model in a graceful way, which is the intrinsical character of the surface flux density noise. Using MC method, we have been developing a virtual optical environment, MOSE, which may employ the 2D/3D analytical models and microCT/MRI slices to define the object geometry[8]. The organs surface of the real mouse above are represented by triangular element to produce the synthetic data in MOSE. The mesh displayed in Fig.2(c) has a maximum element diameter of about $0.6mm$ and is composed of 9000 triangles and 2212 surface measurement points. Optical parameters from the literature [13] and the references therein are assigned to each of the five organ components, as listed in Table I.

B. Source reconstruction

In order to evaluate the proposed adaptive tomographic algorithm, we designed the following experiment. The single bioluminescent source was embedded in the lung as the reconstructed object. In MOSE simulation, a spherical source with the location of $(-4.87, -0.19, 8.77)$ was employed with $1.0mm$ radius and $0.238nano\text{–}Watts/mm^3$ power density, as shown in Fig.3(a). The source was sampled by 1.0×10^6 photons and assumed to obey the uniform distribution. In the reconstruction procedure, The initial coarse volumetrical mesh in Fig.2(d) was entirely different from the mesh used in MOSE and had a maximum element diameter of about $4mm$. The flux density values on the surface points were obtained by the interpolation between the produced point values using MOSE. We set the lower bound S_{inf}^k, the upper bound S_{sup}^k, the gradient tolerance $\varepsilon_g^{(k)}$, the distance tolerance $\varepsilon_d^{(k)}$, and the regularization parameter λ_k to the same values respectively at each level. In addition, we set the mesh refinement ratio r_p, r_f, the maximum number of mesh refinement L_{max} to 50%, 1.5%, 4 respectively. As far as the permissible source region was concerned, the surface light power distribution and the anatomical information of the mouse are shown in Fig.3. Taking into account the FWHM change depending on the source depth in different

TABLE I

Optical parameters of the real mouse.

Material	Muscle	Lung	Heart	Bone	Liver
$\mu_a[mm^{-1}]$	0.01	0.35	0.2	0.002	0.3
$\mu_s[mm^{-1}]$	4.0	23.0	16.0	20.0	6.0
g	0.9	0.94	0.85	0.9	0.9

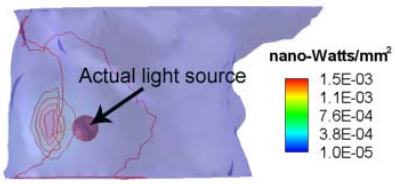

(a)

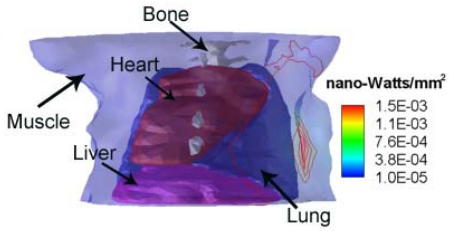

(b)

Fig. 3. The display of the Monte Carlo method based synthetic data. (a) The surface light power distribution of the real mouse versus the actual source position, red lines denote the isoline of the surface light power; (b) That versus the organs location of the mouse.

tissues[14], we selected the domain $P_s = \{(x, y, z)|7.27 < z < 10.27, x < 0.0, (x, y, z) \in Lung\}$ as the permissible source region.

When the initial source density distribution, namely S_1^0, was set to $1.0\times10^{-6} nano–Watts/mm^3$, the reconstruction procedure was terminated via two adaptive mesh evolution. The final reconstructed source is shown in Fig.4(b), which has the maximum source density $0.260 nano–Watts/mm^3$. The relative error (RE) between the actual and reconstructed source is 9.2% when the relative error is defined as $RE = |S_{recons} - S_{real}|/S_{real}$. In view of the location, density and shape of the reconstructed source, the initial coarse mesh based reconstructed results in Fig. 4(a) were gradually near to the actual source through *a posteriori* error estimates and the local mesh refinement.

IV. CONCLUSIONS AND FUTURE WORKS

The preferably quantitative bioluminescent source reconstruction shows the availability and effectiveness of the adaptive finite element tomographic algorithm. The microCT-based anatomical information of the real mouse as *a priori* knowledge helps constrain the number of the BLT possible solutions. The automatically from-coarse-to-fine mesh evolution based on *a posteriori* error estimates further refines the reconstructed light source in view of location, shape and power density. However, although the use of the Monte Carlo method based synthetic data avoids the *inverse crime* to evaluate the performance of the proposed algorithm, many practical factors are not fully taken into account, such as the optical properties of the living small animal, the detection method, and so on. A novel BLT system[16] is being developed, including novel non-contact detection mode[1] and components for diffuse optical tomography, which can reconstruct bioluminescent source with simultaneous optical

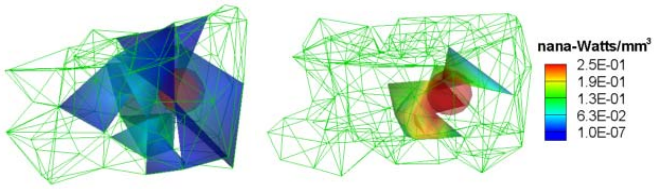

(a) (b)

Fig. 4. Comparison between the actual and reconstructed source. The green mesh denotes the permissible source region; The red sphere is the actual source. (a) The reconstructed results on the initial mesh level; (b) The final results via two adaptive mesh refinement.

properties and high signal-noise-ratio and spatial sampling measured data. Our future work is to test the adaptive tomographic algorithm using the above BLT system and the real mouse experiment. The corresponding results will be reported later.

REFERENCES

[1] V. Ntziachristos, J. Ripoll, L. V. Wang, and R. Weisslder, "Looking and listening to light: the evolution of whole body photonic imaging," *Nature Biotechnology*, vol. 23, no. 3, pp. 313–320, March 2005.
[2] G. Wang, E. A. Hoffman, G. McLennan, L. V. Wang, M. Suter, and J. F. Meinel, "Development of the first bioluminescence ct scanner," *Radiology*, vol. 566, p. 229, 2003.
[3] E. E. Graves, J. Ripoll, R. Weissleder, and V. Ntziachristos, "A submillimeter resolution fluorescence molecular imaging system for small animal imaging," *Medical Physics*, vol. 30, no. 5, pp. 901–911, 2003.
[4] T. F. Massoud and S. S. Gambhir, "Molecular imaging in living subjects: seeing fundamental biological processes in a new light," *Genes and development*, vol. 17, pp. 545–580, 2003.
[5] G. Wang, Y. Li, and M. Jiang, "Uniqueness theorems in bioluminescence tomography," *Medical Physics*, vol. 31, no. 8, pp. 2289–2299, August 2004.
[6] A. J. Chaudhari, F. Darvas, J. R. Bading, R. A. Moats, P. S. Conti, D. J. Smith, S. R. Cherry, and R. M. Leahy, "Hyperspectral and multispectral bioluminescence optical tomography for small animal imaging," *Physics in medicine and biology*, vol. 50, pp. 5421–5441, 2005.
[7] W. Cong, G. Wang, D. Kumar, Y. Liu, M. Jiang, L. V. Wang, E. A. Hoffman, G. McLennan, P. B. McCray, J. Zabner, and A. Cong, "Practical reconstruction method for bioluminescence tomography," *Optics Express*, vol. 13, no. 18, pp. 6756–6771, August 2005.
[8] MOSE, http://www.mosetm.net/.
[9] S. S. Rao, *The finite element method in engineering*. Butterworth-Heinemann, Boston, 1999.
[10] P. E. Gill, W. Murray, and M. Wright, *Practical Optimization*. Academic Press, New York, 1981.
[11] M. Ainsworth and J. T. Oden, A posteriori *error estimation in finite element analysis*. Wiley, 2000.
[12] J. Bey, "Tetrahedral grid refinement," *Computing*, vol. 55, pp. 355–378, 1995.
[13] G. Alexandrakis, F. R. Rannou, and A. F. Chatziioannou, "Tomographic bioluminescence imaging by use of a combined optical-pet (opet) system: a computer simulation feasibility study," *Physics in Medicine and Biology*, vol. 50, pp. 4225–4241, 2005.
[14] B. W. Rice, M. D. Cable, and M. B. Nelson, "*In vivo* imaging of light-emitting probles," *Journal of Biomedical Optics*, vol. 6, no. 4, pp. 432–440, October 2001.
[15] Z. Wu and J. M. Sullivan, Jr., "Multiple material marching cubes algorithm," *International Journal for Numerical Methods in Engineering*, vol. 58, no. 2, pp. 189–207, July 2003.
[16] G. Wang, M. Jiang, J. Tian, W. Cong, Y. Li, W. Han, D. Kumar, X. Qian, H. Shen, T. Zhou, J. Cheng, Y. Lv, H. Li, and J. Luo, "Recent development in bioluminescence tomography," presented in the third IEEE International Symposium on Biomedical Imaging (ISBI 2006), Virginia, USA, 6-9 Apr. 2006.